The Astrophysical Journal, 969:49 (13pp), 2024 July 1 https://doi.org/10.3847/1538-4357/ad47b8

Relativistic Brueckner–Hartree–Fock Calculations for Cold and Hot Neutron Stars

Delaney Farrell[1] and Fridolin Weber[1,2]
[1] Department of Physics, San Diego State University, San Diego, CA 92115, USA; dfarrell@sdsu.edu
[2] Department of Physics, University of California at San Diego, San Diego, CA 92093, USA
Received 2024 February 13; revised 2024 April 30; accepted 2024 May 4; published 2024 June 28

Abstract

This study investigates the properties of symmetric and asymmetric nuclear matter using the relativistic Brueckner–Hartree–Fock formalism, examining both zero and finite temperatures up to 70 MeV. Employing the full Dirac space, we incorporate three Bonn potentials (A, B, and C), which account for meson masses, coupling strengths, cutoff parameters, and form factors. The calculated properties of asymmetric nuclear matter form the basis for constructing equation-of-state (EOS) models tailored for neutron stars. These models, in turn, enable the computation of bulk properties for nonrotating, uniformly rotating, and differentially rotating neutron stars. Notably, the EOS models studied in this paper are sufficiently versatile to accommodate the mass of the most massive neutron star ever detected, PSR J0952–0607, estimated to be $2.35 \pm 0.17\,M_{\odot}$. Furthermore, they yield masses and radii for PSR J0030+451 that align with the confidence intervals established for this pulsar.

Unified Astronomy Thesaurus concepts: Neutron stars (1108); Compact objects (288); Nuclear astrophysics (1129)

1. Introduction

There is a particular interest in the fields of nuclear and astrophysics to learn and model the equation of state (EOS) of nuclear matter under extreme conditions. For superdense nuclear matter, far beyond its saturation point, this knowledge is paramount to the study of neutron stars whose core densities can reach an order of magnitude higher than saturation density. However, the unique internal conditions within a neutron star are well beyond the reach of our terrestrial laboratories, namely due to the extreme densities exhibited in the inner regions of the star and because the matter is highly isospin-asymmetric ($N \neq Z$; Blaschke & Chamel 2018; Lattimer 2019). Some experimental constraints on neutron star matter have come from ultra-relativistic heavy-ion collisions as conducted at the RHIC (Müller & Nagle 2006), the LHC (Aad et al. 2008), and FAIR (Spiller & Franchetti 2006), which probe the nature of hot, symmetric nuclear matter (ANM). Extremely neutron-rich matter has more recently been probed in studies of neutron skin or giant monopole and dipole resonances, but these studies are limited in nature (Roca-Maza et al. 2011). Unfortunately, these experiments currently lack the temperature and density constraints present within the core of a neutron star, meaning the dense matter encountered within a neutron star cannot yet be replicated by experiment. Other promising avenues to constraining the knowledge of the EOS of neutron star matter come from multimessenger astronomy; vital constraints have come from telescopes like the Neutron Star Interior Composition Explorer (NICER; Gendreau et al. 2012) and NASA's Chandra Observatory (Garmire et al. 2003), or, more recently, from the gravitational-wave observatories LIGO (Aasi et al. 2015) and Advanced Virgo (Acernese et al. 2014).

The EOS of dense neutron star matter can be solved theoretically using different nuclear many-body theories which broadly fall into two categories: phenomenological or ab initio. Phenomenological models, based on density functional theories with effective nucleon–nucleon (NN) interactions, are constructed to reproduce the empirical saturation properties of finite nuclei and symmetric nuclear matter (SNM). In contrast to the effective NN interactions used in phenomenological models, ab initio methods employ realistic free-space NN interactions, which are then applied to a nuclear many-body system (see, e.g., Weber 1999; Baldo et al. 2010; Dutra et al. 2012, 2014; Spinella & Weber 2020; Sedrakian et al. 2022, 2023, and references therein.). The parameters of the NN interactions are determined by scattering data of free nucleons and the properties of the deuteron. These interactions are characterized by a repulsive core at short distances, a strong attraction in an intermediate range, and are predominantly influenced by one-pion exchange at large distances.

Most ab initio calculations are constructed in a nonrelativistic framework, which can simulate the saturation behavior of SNM using high-precision, realistic NN potentials (Wang et al. 2020). To reproduce the saturation properties of nuclear matter, nonrelativistic calculations must include the three-body force, which makes calculations to extend the theory to heavier nuclei very difficult. On the other hand, relativistic ab initio methods, like the relativistic Brueckner–Hartree–Fock (RBHF) approximation, can more closely reproduce empirical data than nonrelativistic calculation; a two-body realistic NN potential as a repulsive contribution obtained from the relativistic effect negates the need to include the three-body force (Wang et al. 2021). Solving the nuclear many-body problem in a relativistic framework is considerably more tedious (both theoretically and numerically) than nonrelativistic methods. Because of this, studies carried out using the RBHF approximation have historically been relatively rare in the literature. However, there is a growing body demonstrating that variations of the RBHF approximation are successful in reproducing the empirical saturation properties of SNM and finite nuclei, including the works of ter Haar & Malfliet (1986), Poschenrieder & Weigel (1988), Brockmann & Machleidt (1990), Huber et al. (1995), van Dalen et al. (2007), Shen et al. (2017), Tong et al. (2018), Ring et al. (2021), and Tong et al. (2022).

The vast majority of EOS models for neutron star matter, especially those calculated using a relativistic framework like

the RBHF approximation, are done at zero temperature. However, finite-temperature EOS models are vital to understanding various astrophysical phenomena like core-collapse supernovae, binary neutron star mergers, and proto-neutron stars, as shown in the works of Moustakidis & Panos (2009), Oertel et al. (2017), Carbone & Schwenk (2019), Chesler et al. (2019), Schneider et al. (2019), Koliogiannis & Moustakidis (2021), Wei et al. (2021), and Laskos-Patkos et al. (2022). In this work, we extend the RBHF approximation in full Dirac space to finite temperatures. For ANM, we produce EOS models for dense neutron star matter at both zero and finite temperatures, which are then used to calculate bulk properties of nonrotating, uniformly rotating, and differentially rotating neutron stars. The paper is organized as follows. The theoretical framework of RBHF theory and the modifications for the inclusion of temperature are shown in Section 2. The theoretical framework for calculating the properties of neutron stars, rotating and nonrotating, is discussed in Section 3. Section 4 shows the calculated results, including properties of nuclear matter at zero and finite temperature, and the resulting bulk properties of neutron stars. Section 5 presents a summary of the work.

2. Theoretical Framework: Relativistic Brueckner–Hartree–Fock

The general theory for modeling nuclear matter in the RBHF approximation is outlined in extensive detail in Poschenrieder & Weigel (1988) and Weber (1999), but the essential structure of the approximation is summarized here. Nuclear matter at supranuclear densities can be described from the framework of nuclear physics as a complex, many-body system whose dynamics are governed by the Lagrangian density:

$$\mathcal{L} = \mathcal{L}_N + \sum_M (\mathcal{L}_M + \mathcal{L}_{MN}), \tag{1}$$

where $\mathcal{L}_N$ denotes the Lagrangian of noninteracting nucleons and $\mathcal{L}_M$ is the Lagrangian density of different free-meson fields $M = \sigma, \omega, \rho, \pi, \phi, \delta, \eta$. $\mathcal{L}_{MN}$ describes the interaction between nucleons and mesons; a complete description of the interaction Lagrangians is given in Equations (2.3)–(2.12) in Poschenrieder & Weigel (1988). The interactions caused by various meson fields in the proposed relativistic model are taken into account by an effective relativistic single-particle potential or self-energy (ter Haar & Malfliet 1987). The vital distinction of RBHF theory is that nucleons in this system are treated as effective Dirac particles, described by the Dirac equation.

To describe the properties of a dense, many-body system, the formal structure of the RBHF approach is to solve a highly nonlinear, coupled system of equations. The equations of motion for the various particle fields within the many-body system are derived from the Euler–Lagrange equation and solved with using the Martin–Schwinger hierarchy of coupled Green's functions (Martin & Schwinger 1959). The coupled system of equations involves first determining the two-point Green's function G_1 for all baryons using the Dyson equation:

$$[\not{p} - m - \Sigma(p)]\, G_1(p) = 1, \tag{2}$$

where $\not{p} = \gamma^\mu p_\mu = \gamma^\mu g_{\mu\nu} p^\nu = \gamma^0 p^0 - \sum_{i=1}^{3} \gamma^i p^i$ and γ^0 and γ^i are the Dirac matrices. The influence of the surrounding nucleons is expressed by the nucleon self-energy, $\Sigma(p)$. Once the two-point Green's function is solved for, the in-medium scattering matrix, referred to as the T-matrix, is solved for. It is given by a Bethe–Salpeter-type integral equation:

$$T(P; p, p') = V(p - p') + \int \frac{d^4 p''}{(2\pi)^4} V(p - p'')\, \Lambda \times \left(\frac{P}{2} + p'', \frac{P}{2} - k''\right) T(P; p'', p'), \tag{3}$$

where V is representative of repeated sums of two-particle interactions given by an OBE potential, which describes the interaction among two nucleons in terms of the exchange of scalar, pseudo-scalar, and vector mesons; the matrix elements of the OBE potential V serve as an input to solve the matrix elements of T. The momenta $'p$, p', and p'' denote the relative four-momenta in the final, initial, and intermediate state, respectively, and P is the total momenta. Finally, Λ is the intermediate NN propagator, which takes the form of the Brueckner propagator in the RBHF approach, given by

$$\Lambda(\vec{p}, \vec{p}\,'; P^0) = 2\pi \frac{\Theta(|\vec{p}| - p_F)\, \Theta(|\vec{p'}| - p_F)}{P^0 - \omega_1(|\vec{p}|) - \omega_1(|\vec{p}\,'|)}. \tag{4}$$

Here, the step functions, represented by $\Theta(|\vec{p}| - p_F)$, account for the Pauli exclusion principle, ensuring that intermediate scattering states lie outside the baryon Fermi sea, characterized by the Fermi momentum p_F. As will be discussed in the following section, the step functions are replaced by Fermi–Dirac distribution functions at finite temperatures, given in Equations (10) and (11). The last coupled equation in the formal scheme is for the self-energy (mass operator) Σ, given by an explicit sum over matrix elements, in terms of the T-matrix and the two-point Green's function:

$$\Sigma(p) = \frac{i}{(2\pi)^4} \int d^4 p' \left[\left\langle \frac{p - p'}{2} | T(p + p') | \frac{p - p'}{2} \right\rangle - \left\langle \frac{p - p'}{2} | T(p + p') | \frac{p' - p}{2} \right\rangle \right] G_1(p'). \tag{5}$$

The integral equation that determines the T-matrix, Equation (3), has 256 elements with respect to spin indices, making the computation extremely complicated. A method to simplify the numerical process is to introduce a complete basis of particles (Φ_λ) and antiparticles (θ_λ), where $\lambda = \pm 1/2$ are the helicity eigenvalues. The complete basis is self-consistent, decouples the integral equations, and makes the two-body propagator Λ diagonal. A full description of the self-consistent basis can be found in Poschenrieder & Weigel (1988). The coupled system of equations is derived from momentum-dependent self-energies $\omega(p)$ computed in the full basis, but this procedure can also be made less complicated by using momentum-averaged self-energies (still as a self-consistent calculation). The results shown in Section 4 will compare the full momentum dependence calculations to momentum-averaged calculations.

An elegant technique used to make the many-body equations numerically tractable and to calculate the key quantities of many-body systems is to utilize the spectral representation of the G_1 function (Poschenrieder & Weigel 1988). G_1 can then be

defined in Fourier space at zero temperature as

$$G_1(p) = \int d\omega \, \frac{A(\omega, \vec{p})}{\omega - (p^0 - \mu)(1 + i\eta)}, \tag{6}$$

where A represents the spectral function, which depends on the single-particle energy ω. The quantity μ is the chemical potential of a baryon, and η is used to circumvent a singularity occurring as integrals are carried out in the complex plane. At finite temperatures, the two-point Green's function G_1 is instead expressed as (Huber et al. 1998; Weber 1999)

$$G_1(p^0, \vec{p}) = \int d\omega \, \frac{A(\omega, \vec{p})}{\omega - (p^0 - \mu)(1 + i\eta)} - 2i\pi \mathrm{sign}(p^0 - \mu) \frac{A(p^0 - \mu, \vec{p})}{e^{\beta|p^0 - \mu|} + 1}, \tag{7}$$

with $\beta = 1/k_B T$, where k_B is the Stefan–Boltzmann constant and T is the temperature. While the formal structure of the spectral function A is unaltered when compared to zero temperature, A has an implicit temperature dependence from G_1.

The system of coupled equations follows an iterative process to determine solutions to the above equations. To begin, the self-energy Σ can first be calculated using a simplified approximation like the relativistic Hartree–Fock approach. These calculated values are then used in the first step to determine the spectral functions A and single-particle energies ω. The T-matrix equations can be then solved to determine new values for Σ to be used in the next iterative step until convergence is achieved. Once converged, the properties of nuclear matter (symmetric and asymmetric) which define the EOS can be calculated.

2.1. Properties of Nuclear Matter at Zero and Finite Temperature

When using the spectral representation described in the section above, the properties of nuclear matter can then be determined only by the self-energy Σ and spectral function A (described in greater detail in Poschenrieder & Weigel 1988 and Weber 1999). Once a self-consistent solution to the coupled system of equations is found, bulk properties of SNM can be calculated and compared to empirical values at zero temperature. Using the spectral decomposition of the two-point G_1 function, the number density ρ of the system follows as

$$\rho = \frac{4}{(2\pi)^3} \int d^3p \, A_0(\omega, \vec{p}) \, \Theta(p_F - p), \tag{8}$$

where A_0 is the time-like component of the spectral function and p_F denotes the Fermi momentum. The energy per nucleon E/A of the system is expressed as

$$E/A(\rho) = \frac{1}{4\pi^3} \int d^3p [2(mA_s(p) - pA_v(p)) + \Sigma_s(p)A_s(p - \Sigma_v(p)A_v(p) + \Sigma_0(p)A_0(p))] \, \Theta(p_F - p). \tag{9}$$

In the case of finite temperatures, the step functions Θ seen in Equations (8) and (9) are replaced with Fermi–Dirac distribution functions:

$$f_1(\vec{p}) = \frac{1}{e^{\beta(\omega_1(\vec{p}) - \mu)} + 1}, \tag{10}$$

$$f_2(\vec{p}) = \frac{1}{e^{\beta(-\omega_2(\vec{p}) + \mu)} + 1}, \tag{11}$$

where "1" indicates the positive-energy states and "2" indicates the thermally excited negative-energy states. We remember that at finite temperatures, the behavior of nuclear matter undergoes important modification, attributed to thermal baryonic excitations surpassing the Fermi surface. Contrary to absolute-zero conditions where all states within the Fermi sea ($|\vec{p}| < p_F$) are fully occupied, higher temperatures induce partial occupancy due to thermal excitations of positive- and negative-energy states. This phenomenon significantly impacts various thermodynamic attributes of dense stellar matter, including the EOS and the entropy of hot neutron star matter. Both positive- and negative-energy state distributions adhere to modified Fermi–Dirac statistics, resulting in alterations in state occupancy for both species, both below and above the Fermi surface, as expressed by Equations (10) and (11). As $T \to 0$, the Fermi–Dirac distribution for positive-energy states becomes

$$f_1(\vec{p}) \to \Theta(\mu - \omega_1(\vec{p})), \tag{12}$$

and for negative-energy states $f_2 \to 0$.

Once the energy per nucleon and number density of the system are calculated, the compressibility K of the matter can be calculated as

$$K(\rho) = 9\rho^2 \left(\frac{\partial^2 E/A(\rho)}{\partial \rho^2} \right). \tag{13}$$

At zero temperature, the pressure P is also computed from E/A:

$$P(\rho) = \rho^2 \left(\frac{\partial E/A(\rho)}{\partial \rho} \right). \tag{14}$$

For finite temperatures, the pressure is instead determined by calculating the free energy per nucleon, denoted as F/A, which is defined as

$$F(\rho, T) = U(\rho, T) - TS(\rho, T), \tag{15}$$

where U is the internal energy (equal to the energy per nucleon E/A with the thermal contribution) and S is the entropy of the system (ter Haar & Malfliet 1986). The entropy is given by

$$S(\rho, T) = \frac{-1}{(2\pi)^3 \rho} \int d^3p \, [(1 - f)\ln(1 - f) + f \ln(f)], \tag{16}$$

where f is the Fermi–Dirac distribution. Both positive- and negative-energy states contribute to S, but the negative-energy contribution is very small ($f_2 << f_1$). Therefore, Equation (16) can be approximated with only the positive-energy state contribution, or $f = f_1$. In the results presented in this work, the temperature is held fixed and entropy calculated. The numerical procedure can be completed by instead holding entropy fixed; see Farrell et al. (2023), for an example. Once the entropy S, and subsequently the free energy F, are

calculated, the pressure is derived at finite temperatures as

$$P(\rho, T) = \rho^2 \frac{\partial F(\rho, T)}{\partial \rho}. \quad (17)$$

The total energy density ϵ of the system follows from the energy per baryon as

$$\epsilon(\rho) = (E/A(\rho) + m)\,\rho, \quad (18)$$

where m is the nucleon mass.

In the case of ANM, an asymmetry parameter α, which defines the asymmetry between the number of neutrons and protons in the system, can be defined as

$$\alpha = \frac{\rho_n - \rho_p}{\rho}, \quad (19)$$

where ρ_n is the density of neutrons and ρ_p is the density of protons. In the case of SNM, $\alpha = 0$, and for pure neutron matter (PNM), $\alpha = 1$. For ANM, the energy per nucleon can be expressed as a power series dependent on the total density of the system ρ and the asymmetry parameter α (Tong et al. 2022):

$$E/A(\rho, \alpha) = E/A(\rho, 0) + E_{\rm sym}(\rho)\alpha^2 + \mathcal{O}(4). \quad (20)$$

$E_{\rm sym}$ is the nuclear symmetry energy, which is defined as

$$E_{\rm sym}(\rho) = \frac{1}{2}\frac{\partial^2 E/A(\rho, \alpha)}{\partial \alpha^2}|_{\alpha=0}, \quad (21)$$

and can be approximated as $E_{\rm sym}(\rho) \approx E/A(\rho, 1) - E/A(\rho, 0)$ (Li et al. 2021).

3. Theoretical Framework: Neutron Star Properties

The EOS of neutron star matter is described as a relationship between the pressure P and energy density ϵ of the many-body system within. This holds for the majority of neutron stars, which can be described as zero temperature on the nuclear scale (just a few MeV). However, following extreme events like a core-collapse supernova or a binary neutron star merger, the temperature of the system is much higher (on the order of 50–100 MeV) and therefore plays a critical role in the EOS. The RBHF formalism is used to calculate the EOS of ANM within a neutron star at both zero and finite temperatures. Once an EOS model has been defined, the structural properties of a neutron star can be calculated in the framework of Einstein's theory of general relativity.

3.1. Nonrotating Stars

For nonrotating stars, the stellar structure is described by the Tolman–Oppenheimer-Volkoff equation (assuming $G = c = 1$; Tolman 1939):

$$\frac{dP(r)}{dr} = -\frac{(\epsilon(r) + P(r))(m(r) + 4\pi r^3 P(r))}{r^2\left(1 - \frac{2m(r)}{r}\right)}, \quad (22)$$

which describes the pressure gradient within the star as a function of the radius r. The gravitational mass $m(r)$ contained in a sphere of radius r can be found with

$$\frac{dm}{dr} = 4\pi r^2 \epsilon(r), \quad (23)$$

where at the origin $m(0) = 0$. Using a specified model for the EOS, a star's mass and radius can be determined by first choosing a central value for density ϵ_C with a corresponding pressure value P_C, and integrating Equations (22) and (23) until pressure vanishes, signifying the total radius R of the star.

3.2. Rotating Stars

The stellar structure of rotating stars is more complicated than that of nonrotating stars for several reasons. Nonrotating stars are assumed to be spherically symmetric, so their stellar structure depends solely on the radial coordinate. However, rapid rotation can deform the star's shape by flattening at the pole and expanding in the equatorial direction; to account for this deformation, the stellar structure equations must also include a dependence on the polar coordinate θ. While spherical symmetry is broken in rotating stars, the assumptions of stationary rotation, axial symmetry, and reflection symmetry still hold, leaving the stellar structure equations independent from time t and the azimuthal angle ϕ. The metric of a rotating neutron star can thus be written as

$$ds^2 = -e^{2\nu}(dt)^2 + e^{2\psi}(d\phi - \omega dt)^2 + e^{2\mu}(d\theta)^2 + e^{2\lambda}(dr)^2, \quad (24)$$

where the metric functions (ν, ψ, μ, and λ) are dependent on the radial r and polar θ coordinates, as well as implicitly on the star's rotational frequency Ω. The term ω is indicative of an additional complication from rotation: the general relativistic effect of frame dragging, where ω is the angular velocity of the local inertial frames being dragged in the direction of the star's rotation.

The vast majority of rotating neutron stars are believed to be rotating uniformly or as a rigid body. The absolute upper limit for a uniformly rotating neutron star's rotational frequency is the mass-shedding limit, set by the Kepler frequency Ω_K. This frequency can be defined in terms of the metric functions ψ and ν, and the frame-dragging term ω as

$$\Omega_K = \frac{\omega'}{2\psi'} + e^{\nu-\psi}\left[\frac{\nu'}{\psi'} + \left(\frac{\omega'}{2\psi'}e^{\psi-\nu}\right)\right]^{1/2} + \omega, \quad (25)$$

and mass-shedding occurs when the angular velocity reaches Ω_K at the star's equator. In general, rotating stars have the capacity to be more massive than nonrotating stars, as rotation stabilizes the star against gravitational collapse. The mass-shedding limit sets the maximum allowed mass of a uniformly rotating neutron star, which can be 20% higher than nonrotating stars for very stiff EOS models (Lyford et al. 2003).

Following extreme astrophysical events like binary neutron star mergers, neutron stars may instead form with an appreciable amount of differential rotation due to complicated hydrodynamic motions during the coalescence. In addition to rotating differentially, remnant objects are expected to be extremely hot, with temperatures on the order of 50–100 MeV (Perego et al. 2019). The physical implications of differential rotation paired with thermal pressure allow stars to remain stable in otherwise unstable configurations. Most notably, differential rotation provides centrifugal support to stabilize the star at higher masses than their uniformly rotating or nonrotating counterparts, giving rise to so-called hypermassive remnant stars (Morrison et al. 2004).

Table 1
Saturation Properties of SNM at Zero Temperature for Different Approximations Using the Bonn Potentials (A, B, and C)

Method for Self-energy Σ	Potential	ρ_0 (fm^{-3})	E/A (MeV)	p_F (fm^{-1})	K (MeV)	m^*/m	$E_{\rm sym}$ (MeV)
Momentum-dependent	A	0.17	−14.08	1.36	281.64	0.675	32.07
	B	0.16	−12.99	1.33	246.77	0.701	29.67
	C	0.15	−12.30	1.30	227.99	0.725	27.26
Momentum averaged	A	0.17	−15.45	1.36	265.54	0.657	33.44
	B	0.16	−14.33	1.33	241.40	0.685	31.01
	C	0.16	−13.63	1.33	225.31	0.692	28.86
Empirical value		0.15–0.16	−15–17	1.32	220–260	0.7–0.9	32

Note. The first approximation is carried out using a momentum-dependent self-energy, and the second uses a momentum-averaged self-energy. Empirical value ranges are shown in the last row; see text for discussion and references.

Due to the complications introduced by rotation, there exists no analytical solution for solving the system of equations deriving the stellar structure of relativistic rotating objects. Instead, numerical methods are employed. An in-depth review of different schemes used to model uniformly rotating stars can be found in Stergioulas (2003). For the context of this work, models for uniformly rotating stars at the Kepler frequency are computed using Hartle's perturbative rotation formalism (Weber & Glendenning 1992). The formalism described in Cook et al. (1992, 1994) is employed to model differential rotation in neutron stars. This formalism requires the choice of a rotation law to describe the differential rotation profile; we follow Cook et al. (1992) by choosing the following linear rotation law:

$$F(\Omega) = A^2(\Omega_c - \Omega), \tag{26}$$

where Ω is the nonconstant angular velocity and Ω_c is its central value. The parameter A is used to determine the length scale over which the frequency changes, and acts as a scaling factor of the degree of differential rotation (Morrison et al. 2004). In practice, it is convenient to parameterize calculations using a version of this parameter scaled by the equatorial radius, $\hat{A}^{-1} = r_e/A$, where uniform rotation is obtained in the limit $\hat{A}^{-1} \to 0$.

4. Results and Discussions

The saturation properties of dense SNM and ANM are calculated at zero and finite temperatures. For this investigation, calculations are carried out using the three OBE potentials constructed by Brockmann and Machleidt (Brockmann & Machleidt 1990), known colloquially as the Bonn potentials (denoted by A, B, and C). The calculated EOS models are then used to determine the bulk properties of neutron stars.

4.1. Properties of Dense Matter at Zero Temperature

The Bonn potentials have previously been shown to produce values for the bulk properties of SNM at zero temperature that are in good agreement with empirical values (Brockmann & Machleidt 1990; Huber et al. 1995; Weber 1999; Tong et al. 2022). For both the full momentum dependence and the momentum-averaged calculations, values for the saturation density ρ_0, energy per nucleon E/A, Fermi momentum p_F, compressibility K, effective nucleon mass m^*/m, and symmetry energy $E_{\rm sym}$ are given in Table 1. The corresponding empirical values are shown for comparison, but it is worth noting the empirical values for the saturation properties vary across the literature.

The saturation density, ρ_0, is found in a recent study to be within the range 0.15–0.16 fm^{-3} (Lattimer 2023). This value directly correlates to the Fermi momentum p_F via

$$\rho_0 = \frac{2p_F^3}{3\pi^2}, \tag{27}$$

leading its empirical value to be ≈1.32 fm^{-1}. The energy per nucleon E/A is also given in Lattimer (2023) to fall within the range −15 to −17 MeV, but has been found with different bounds throughout the literature. For the compressibility K, Stone et al. (2014) provides a historical overview of the empirical range from a variety of theoretical approaches, which is shown to be as low as 100 and as high as 370 depending on the reference. However, more recent studies like that of Garg & Colo (2018) provide a more narrow uncertainty band on K, giving the credible range of 220–260 MeV. For the effective nucleon mass m^*/m, analyses of the isoscalar nucleon mass provide the range 0.7–0.9, but there is less consensus of the isovector nucleon mass, with values ranging as low as 0.6 and as high as 0.93 (Li et al. 2018). Baldo & Burgio (2016) provide values for the symmetry energy $E_{\rm sym}$ using different semiclassical methods but finds a consensus centered around 32 MeV.

Figure 1 depicts the energy per nucleon for the momentum-dependent and momentum-averaged calculations resulting from the three Bonn potentials. For both methods, the Bonn potential A results are the closest to the empirical value for the binding and symmetry energies, a finding that is consistent with other implementations of the RBHF approximation. The calculated compressibilities and effective masses for the three Bonn potentials spread over a wide range of values; these two parameters historically have had less consensus for their respective credible ranges, so the larger distribution of values is unsurprising.

We next investigate ANM produced by the RBHF approximation in order to produce an EOS for neutron star matter. For ANM, results are shown for the full iteration procedure using the momentum-dependent Σ. Following the theoretical description in Section 2.1, the energy per nucleon E/A of ANM, defined in Equation (20), becomes dependent on the asymmetry

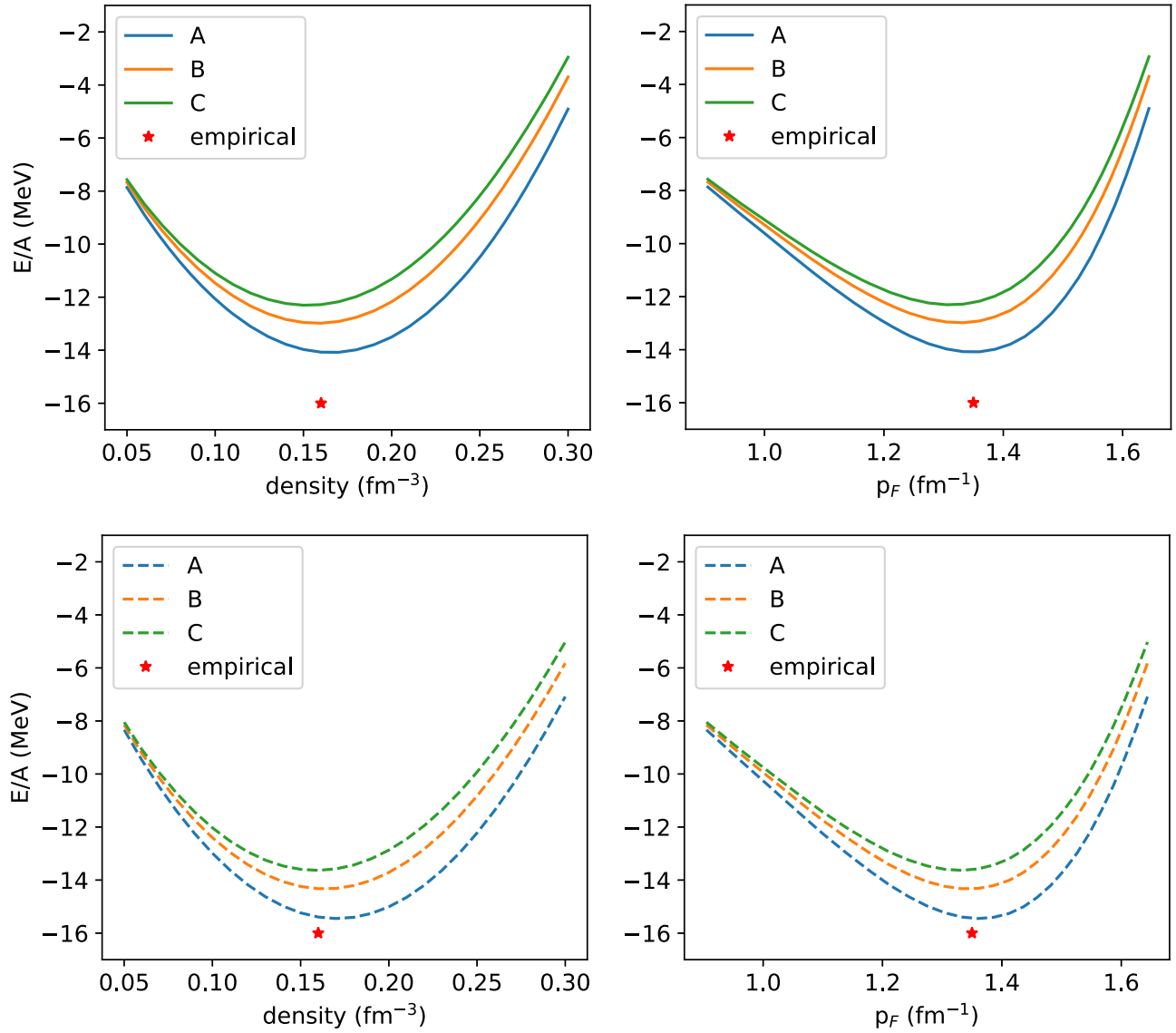

Figure 1. The energy per nucleon E/A for the three Bonn potentials (A, B, and C) compared to density ρ on the left and Fermi momentum p_F on the right. The top row with solid lines shows the momentum-dependent self-energy approximation completed in the full basis, and the bottom row with dashed lines is the momentum-averaged approximation.

parameter α. When $\alpha = 0$, there are an equal number of protons and neutrons within the system (SNM), and when $\alpha = 1$, the system is PNM. In Figure 2, energy per nucleon is shown as a function of density for varying values of α, along with the calculated results of Akmal et al. (1998), known colloquially as APR.

In the high-density regime of a neutron star, the asymmetry between neutrons to protons is believed to be $\approx$0.8. Using the energy per nucleon E/A with $\alpha = 0.8$ and the corresponding number density ρ, the pressure P and energy density ϵ can be calculated using Equations (14) and (18), respectively. The EOS models for the Bonn potentials A, B, and C following this procedure are displayed in Figure 3. Despite the differences in the saturation properties of the three potentials, the resulting EOS models remain very similar.

4.2. Properties of Dense Matter at Finite Temperature

We extend the calculations of nuclear matter in the RBHF approximation to finite temperatures, specifically for $T = 10$, 30, 50, and 70 MeV. Modifications to the numerical scheme are introduced to be consistent with the mathematical framework described in Section 2.1. Due to the additional complexity of the algorithm, we find solutions to be more stable numerically, especially at higher temperatures, using the momentum-averaged self-energy approximation.

The binding energies per nucleon E/A for four different temperatures are shown in Figure 4, calculated using the Bonn B potential. Each meson provides a thermal contribution to the energy per nucleon, which grows larger as the temperature increases. For finite temperatures, the energy per nucleon is used to calculate the free energy per nucleon F/A, given in Equation (15). When using the RBHF approximation at temperatures $\geqslant$50 MeV, we find the Bonn B potential provided the most stable results. The free energies of SNM and PNM from the Bonn B potential for four temperatures are displayed in Figure 5.

Pressure is calculated from F/A using Equation (17). As for zero temperature, the pressure and energy density are calculated with the asymmetry parameter $\alpha = 0.8$ for neutron

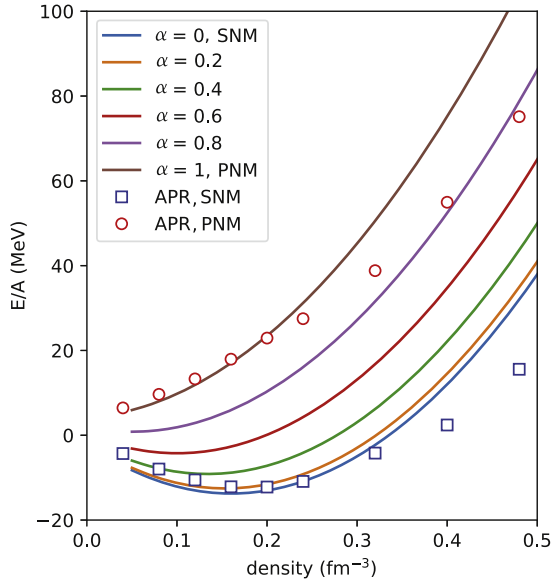

Figure 2. Energy per nucleon E/A vs. density for ANM calculated with the Bonn A potential at zero temperature. Shown are varying values of the asymmetry parameter α ranging from 0 (SNM) to 1 (PNM), and compared to the APR method shown with blue squares (SNM) and red circles (PNM).

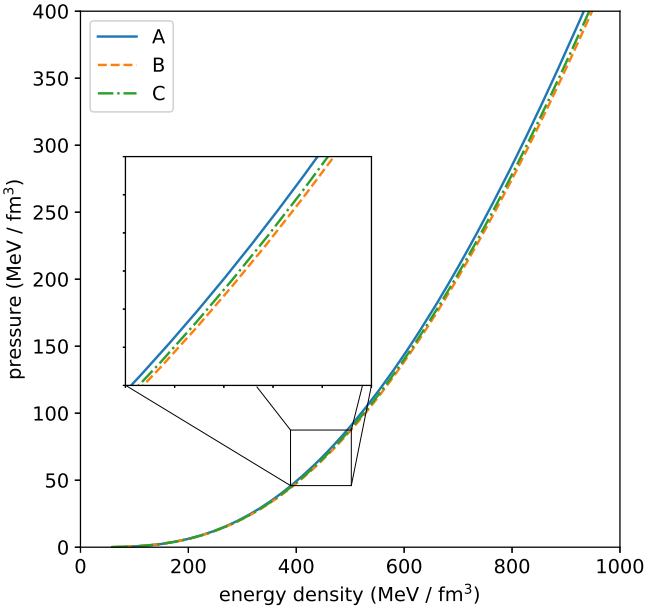

Figure 3. Pressure P as a function of energy density ϵ for all three Bonn potentials (A, B, and C) for ANM with $\alpha = 0.8$ (see text for more details).

star matter. The EOS, pressure vs. energy density, for varying temperatures are shown in Figure 6. Temperature stiffens the resulting EOS. Higher temperatures at low densities introduce some level of numerical noise, as seen in Figure 6.

4.3. Nonrotating and Uniformly Rotating Neutron Star Properties

Once models have been defined for the EOS of neutron star matter at both zero and finite temperatures, bulk properties like mass and radius can be solved numerically.

At zero temperature, EOS models resulting from both the momentum-dependent and momentum-averaged self-energy calculations are used. To compute rotating and nonrotating stellar models, an EOS that describes the neutron star from the core to the crust must be specified. The RBHF approximation is used for the high-density region. For the crust, we use Harrison and Wheeler (Harrison et al. 1965, hereafter HW) for the outer crust, and Negele and Vautherin (Negele & Vautherin 1973, hereafter NV) for the inner. Mass–radius relations for nonrotating (dashed lines) and uniformly rotating (solid lines) stars are shown in Figure 7, resulting from calculations that use the momentum-dependent self-energy in the full basis for the Bonn A, B, and C potentials. For all three models, the rotating mass–radius relations are shown at their mass-shedding or Kepler limit ($\Omega = \Omega_K$). Additionally shown are the confidence intervals for the mass and radius of PSR J0030+451, observed by NICER and analyzed in Miller et al. (2019). The outer contour is the 68% interval and the inner is 95%. Both the nonrotating and rotating mass–radius relations fall in the 95% confidence interval for all three potentials.

Bulk properties of nonrotating and uniformly rotating stars (at their mass-shedding limit) constructed with the zero-temperature EOS models are given in Table 2. For both nonrotating and rotating stars, the maximum mass $M_{\rm max}$ and corresponding radius $R_{\rm max}$ are shown. For both nonrotating and rotating stars, the maximum masses shown in Table 2 are both over 2 $M_\odot$, as required by observational constraints. This is unsurprising given the framework discussed in Section 2 accounts only for purely nucleonic matter. A discussion of the inclusion of other baryons, specifically hyperons, and their importance in describing a realistic depiction of neutron star interiors is given in Section 5. Additionally, the Kepler frequency Ω_K and stability parameter $T/|W|$ are provided for the uniformly rotating stellar models. The stability parameter is the ratio of rotational (T) to gravitational (W) energy. Stability studies have previously specified the limit of $T/|W| < 0.14$ for uniformly rotating stars to remain stable against secular instabilities, and previous work finds this parameter in the range $0.11 < T/|W| < 0.13$ for stars rotating at their respective Kepler frequencies (Weber et al. 1991; Ou et al. 2004). For the three Bonn potentials, both the momentum-dependent and momentum-averaged approximations fall within the stable range.

For finite temperatures, only models constructed using the momentum-averaged self-energy approximation are used, as discussed in Section 4.2. To solve for stellar models, the high-density, finite-temperature EOS must also be fit to an EOS for the crust. Popular models for neutron star crusts, like the previously mentioned HW+NV, are all constructed at zero temperature, meaning there is a discontinuity in the temperature for the low-density and high-density regions of the star. In massive neutron stars, the crust regions are thin and contribute negligibly to the bulk properties like mass (Weber 1999), but the connection of the zero-temperature crust to the finite-temperature core can skew the determination of the radius. For this reason, we focus only on higher-mass stars created by fitting the finite-temperature EOS models constructed using the RBHF approximation to the zero-temperature HW+NV EOS for the crust.

Mass compared to central energy density ϵ_c for four temperatures ($T = 10$, 30, 50, and 70 MeV) are shown in Figure 8, calculated using the Bonn B potential. As mentioned previously, the low-density portion of the higher-temperature EOS models, especially $T = 70$ MeV, do not have good agreement with the zero-temperature HW+NV EOS, which can be seen for the low-mass stars in Figure 8. As with the

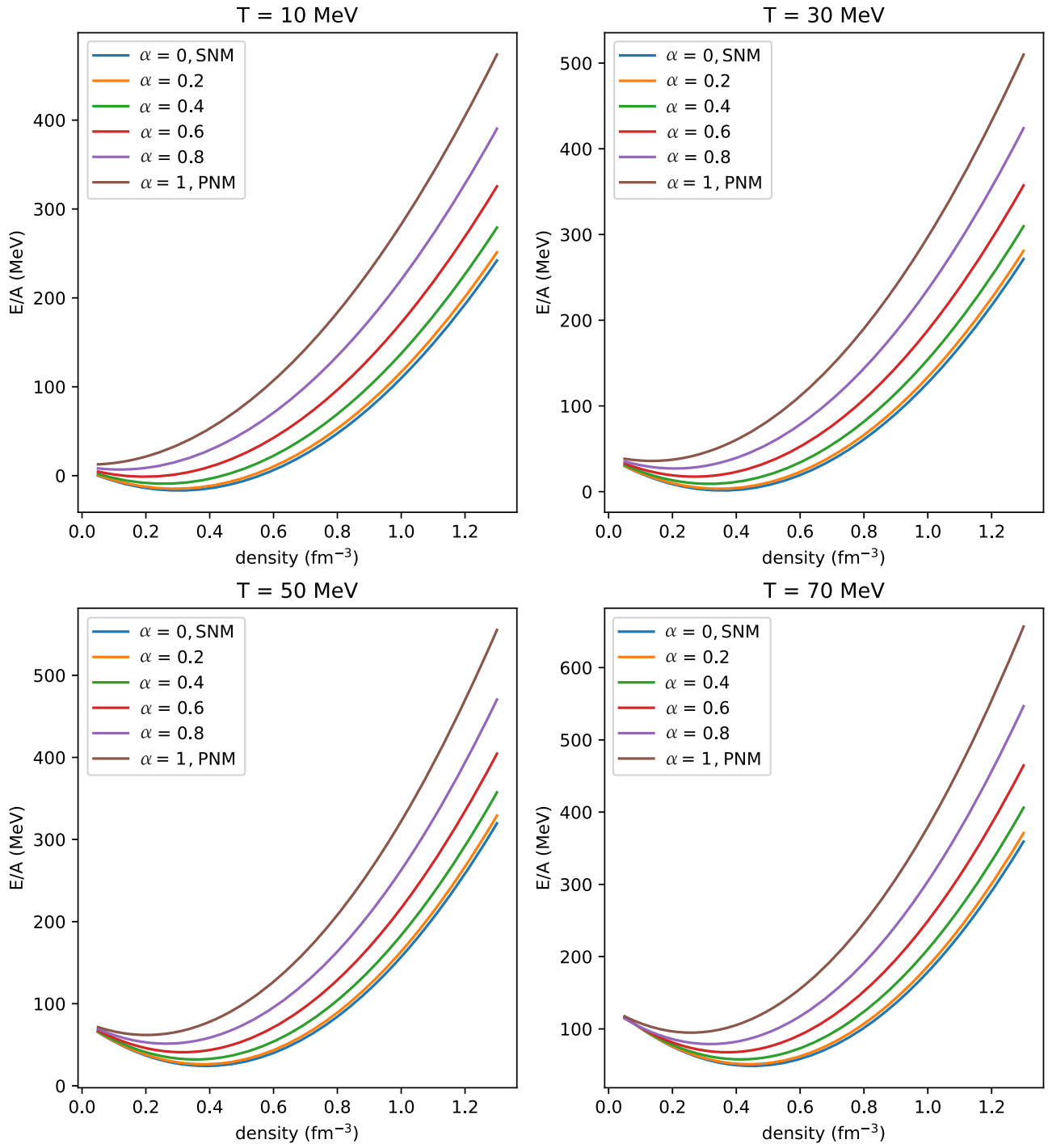

Figure 4. Energy per nucleon E/A vs. density of ANM calculated with the Bonn B potential for four different temperatures: 10, 30, 50, and 70 MeV. For each temperature, the asymmetry parameter α ranges from 0 (SNM) to 1 (PNM).

zero-temperature constructed EOS models, the bulk properties of nonrotating and uniformly rotating neutron stars constructed with the finite-temperature EOS models using the Bonn B potential are displayed in Table 3. Even with high temperatures, the stability parameter $T/|W|$ remains in the specified range of $0.11 < T/|W| < 0.13$ for stars rotating at their respective Kepler frequencies. Increasing the temperature leads to higher-mass peaks, as shown in Table 3, but has an inverse effect on the Kepler frequency Ω_K. When compared to the zero-temperature EOS from the Bonn B potential using the momentum-averaged Σ in the RBHF approximation, the EOS at 70 MeV sees a 19.1% increase in mass for nonrotating stars and a 17.3% increase for uniformly rotating stars.

4.4. Differentially Rotating Neutron Star Properties

As discussed in Section 3.2, hypermassive neutron stars may form with a considerable degree of differential rotation following high-energy events like the merging of two neutron stars. Differential rotation paired with thermal pressure from high temperatures allows these stars to sustain total masses considerably higher than both nonrotating and uniformly

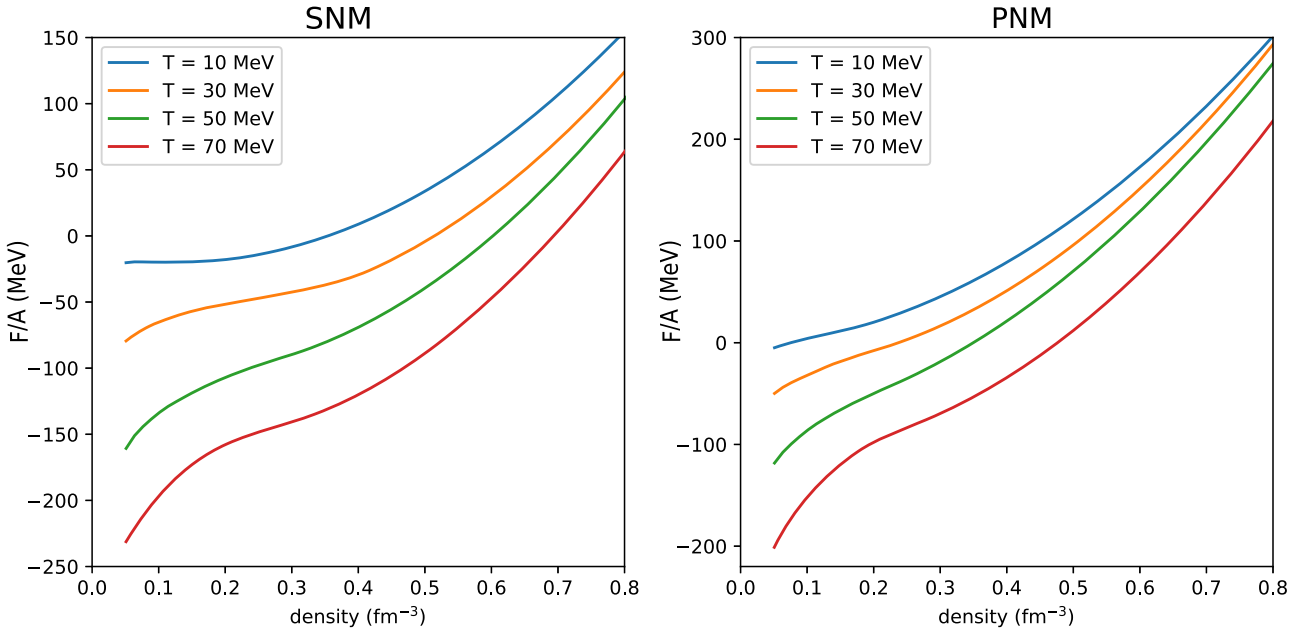

Figure 5. Free energy per nucleon F/A vs. density for SNM (left panel) and PNM (right panel) calculated with the Bonn B potential. The plots show results for four temperatures: 10, 30, 50, and 70 MeV.

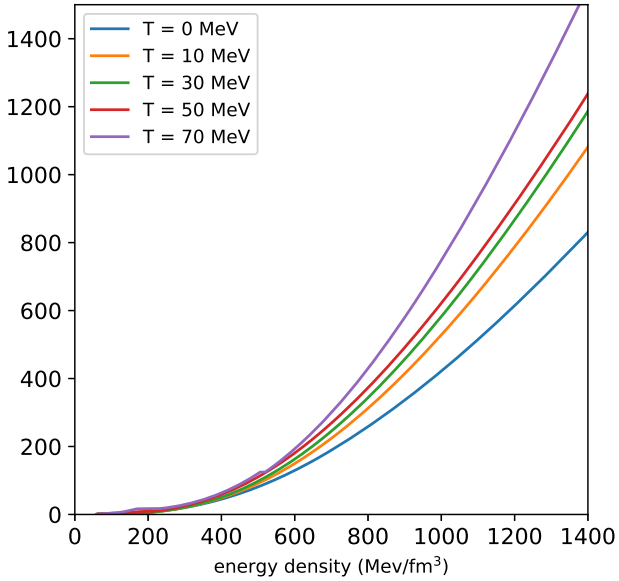

Figure 6. Pressure P as a function of energy density ϵ calculated with the Bonn B potential for ANM with $\alpha = 0.8$. Shown are the zero-temperature EOS and four models at temperatures 10, 30, 50, and 70 MeV.

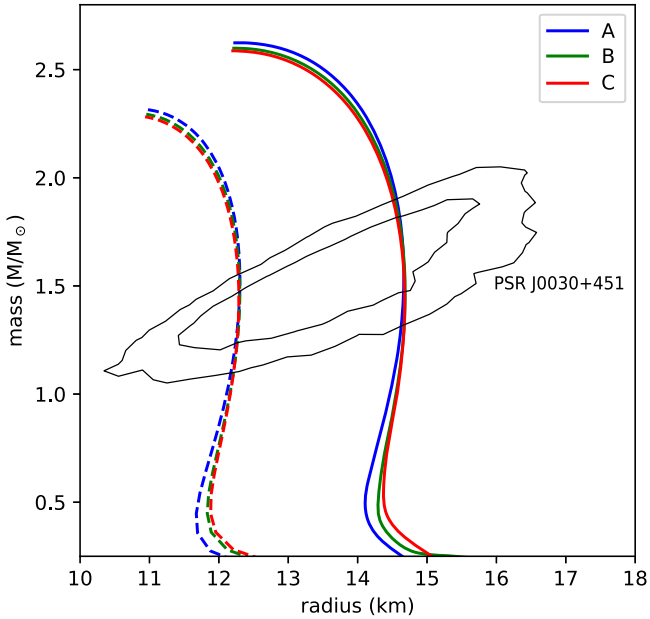

Figure 7. Mass–radius relations for rotating (solid lines) and nonrotating (dashed lines) neutron stars from EOS models computed with the RBHF approximation at zero temperature using the Bonn A, B, and C potentials. Computations use the full basis and a momentum-dependent self-energy (see text for more details). The black contours show the confidence intervals for the mass and radius of PSR J0030+451 (Miller et al. 2019).

rotating stars. These massive, differentially rotating neutron stars may also deviate from spherical or axial symmetry by exhibiting extreme triaxial deformations. The structural deformation and differential rotation allow the compact remnant to remain stable on short, dynamical timescales, for masses that would render configurations unstable in the static and uniform-rotation cases. The four finite-temperature EOS models are used to determine bulk properties of differentially rotating stars. In this section, we focus on the increase in mass from uniform rotation as well as the potential structural deformation caused by a high degree of differential rotation.

Mass compared to central energy density ϵ_c of differentially rotating stars at four temperatures ($T = 10$, 30, 50, and 70 MeV) are shown in Figure 9, calculated using the Bonn B potential. The differentially rotating models are constructed for a high degree of differential rotation, characterized by setting the rotation parameter $\hat{A}^{-1} = 1.0$. For high degrees of differential rotation, the stellar sequence finds a maximum at a lower central density when compared to uniform rotation for all four temperatures, and can fall below the mass-shedding limit at higher densities. This trend is seen in other implementations of the numerical scheme used (Morrison et al. 2004). Additionally, as temperature increases, stable

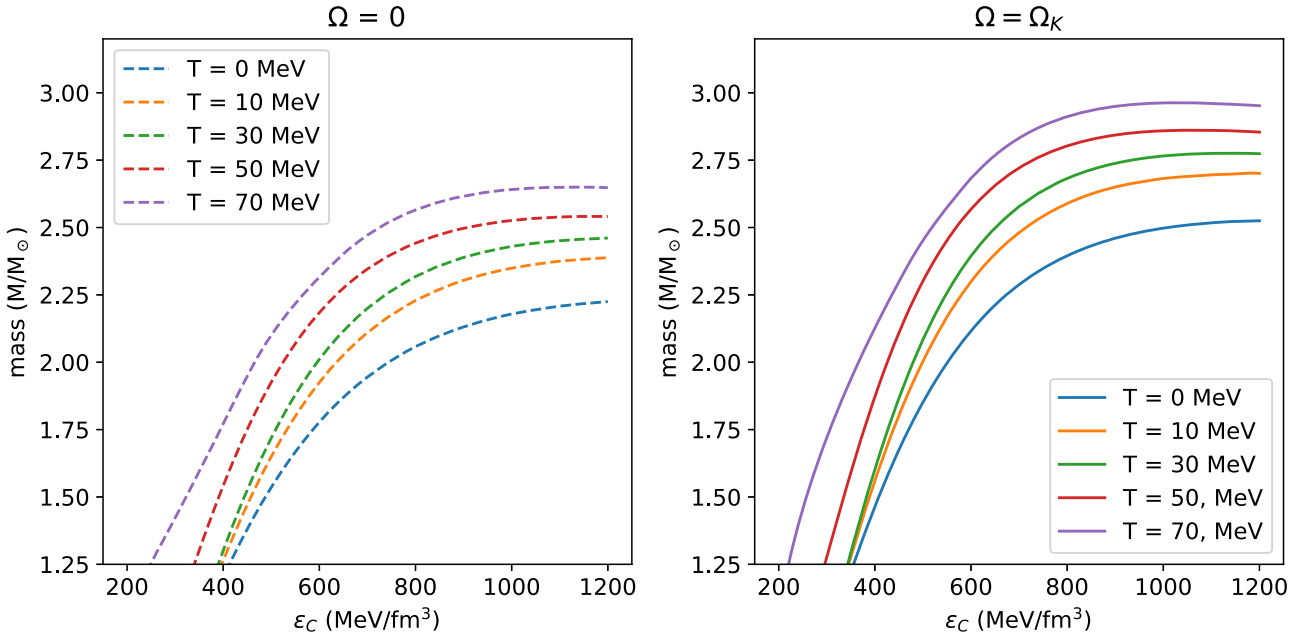

Figure 8. Mass vs. central density ϵ_C from EOS models computed with the RBHF approximation at a range of temperatures ($T = 10$, 30, 50, and 70 MeV) using the Bonn B potential. Nonrotating stellar models are shown on the left (dashed lines) and uniformly rotating models at the mass-shedding limit are shown on the left (solid lines).

Table 2
Nonrotating and Uniformly Rotating Neutron Star Properties Calculated with the Zero-temperature EOS Models from the RBHF Approximation, Using the Three Bonn Potentials

		Nonrotating ($\Omega = 0$)		Rotating ($\Omega = \Omega_K$)			
Method for Self-energy Σ	Potential	$M_{\max}$ ($M_\odot$)	$R_{\max}$ (km)	$M_{\max}$ ($M_\odot$)	$R_{\max}$ (km)	Ω_K (Hz)	$T/\lvert W\rvert$
Momentum dependent	A	2.315	10.978	2.624	12.230	1916	0.116
	B	2.294	10.954	2.599	12.261	1908	0.115
	C	2.282	10.937	2.587	12.248	1900	0.115
Momentum averaged	A	2.237	10.861	2.538	12.186	1910	0.114
	B	2.225	10.855	2.525	12.140	1906	0.114
	C	2.203	10.824	2.501	12.117	1904	0.113

Note. Results are shown for EOS models constructed with momentum-dependent and momentum-averaged self-energy Σ. Bulk properties include the maximum mass $M_{\max}$and corresponding radius $R_{\max}$for both nonrotating and rotating stars, as well as the Kepler frequency Ω_K and stability parameter $T/|W|$ for rotating stars.

Table 3
Nonrotating and Uniformly Rotating Neutron Star Properties Calculated with EOS Models at Finite Temperatures from the RBHF Approximation, Using the Bonn B Potential

	Nonrotating ($\Omega = 0$)		Uniformly Rotating ($\Omega = \Omega_K$)			
Temperature (MeV)	$M_{\max}$ ($M_\odot$)	$R_{\max}$ (km)	$M_{\max}$ ($M_\odot$)	$R_{\max}$ (km)	Ω_K (Hz)	$T/\lvert W\rvert$
10	2.388	10.900	2.702	12.112	1967	0.120
30	2.461	10.973	2.776	12.238	1958	0.122
50	2.541	11.439	2.861	12.887	1844	0.119
70	2.650	11.819	2.963	13.277	1803	0.113

Note. Bulk properties include the maximum mass $M_{\max}$ and corresponding radius $R_{\max}$for both nonrotating and rotating stars, as well as the Kepler frequency Ω_K and stability parameter $T/|W|$ for uniformly rotating stars.

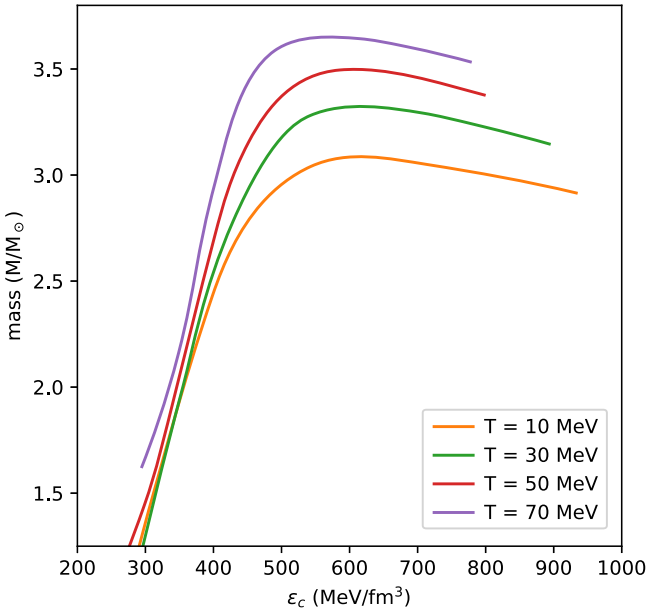

Figure 9. Mass vs. central density ϵ_C for differentially rotating stellar models from EOS models computed with the RBHF approximation at a range of temperatures ($T = 10$, 30, 50, and 70 MeV) using the Bonn B potential. The differentially rotating models are constructed with a high degree of differential rotation where the rotation parameter $\hat{A}^{-1} = 1.0$; see text for more details.

solutions are restricted to lower central densities, as shown in Figure 9. For the calculated models, there is a significant increase in the maximum mass for the differentially rotating models constructed with $\hat{A}^{-1} = 1.0$ when compared to the uniformly rotating sequences at their respective mass-shedding limit. There is an 11.8% increase in maximum mass for a temperature $T = 10$ MeV, an 18.8% increase for $T = 30$ MeV, a 21.1% increase for $T = 50$ MeV, and a 21.4% increase for $T = 70$ MeV. The increase in mass is largely dependent on the rotation parameter $\hat{A}^{-1}$ and, in turn, the choice of rotation law. As discussed in Section 3.2, the results displayed here use a linear rotation law (the so-called "j-constant law"), though other studies, like that in Hanauske et al. (2017), find nonlinear rotation laws may be better suited to describe the rotation profile of a hypermassive remnant star

Structural deformation from rapid uniform rotation has been demonstrated through numerical simulation rapid rotation (Hartle & Thorne 1968; Huber et al. 1998; Weber 1999) to result in a lengthening of the radius at the equator and shortening at the pole. In the case of differential rotation, more extreme structural deformations can occur as the ratio of polar to equatorial radius in the star tends toward zero, in some cases leading to the formation of toroidally shaped objects (Lyford et al. 2003; Morrison et al. 2004). Using the EOS model at $T = 70$ MeV, density and frequency contour plots are shown in Figure 10 constructed with a rotation parameter $\hat{A}^{-1} = 1.0$. This stellar model has a quasi-toroidal shape as shown by the density contours, where the densest regions of the star are beginning to shift from the center. The high degree of differential rotation is demonstrated in the frequency map, where the range of frequency within the star spans 3600 Hz.

5. Summary and Conclusions

In this paper, we present a comprehensive investigation into the properties of SNM and ANM, employing self-consistent calculations utilizing the effective scattering matrix within the full Dirac space, following the methodology outlined in Poschenrieder & Weigel (1988) and Weber (1999). Specifically, we utilized the Bonn potentials (A, B, and C) for the OBE interaction. Our study begins with the examination of SNM, where we conduct calculations of saturation properties at zero temperature, yielding results that align well with empirical values from diverse sources. Subsequently, our analysis extends to ANM, as detailed in Section 2.1, laying the groundwork for constructing EOS models pertinent to neutron star matter.

Expanding our investigation to include finite temperatures, we adapted the two-point Green's function within the RBHF scheme, as elucidated in Section 2.1. Here, employing the Bonn B potential, we derive results up to 70 MeV. We highlight here that when modeling certain hot astrophysical systems, like the remnant star formed from a binary neutron star merger event, temperatures above 70 MeV may be necessary. The results presented in this work are, however, limited by the stability of the numerical scheme, and future work should entail studies at higher temperatures. Analogous to our zero-temperature analysis, the properties of ANM at finite temperatures serve as the foundation for constructing EOS models tailored to varying temperature regimes relevant to neutron stars.

Subsequently, we leveraged the zero- and finite-temperature EOS models to compute bulk properties of both nonrotating and rotating neutron stars, with uniformly rotating models computed up to the mass-shedding limit ($\Omega = \Omega_K$). Our investigation reveals that while the saturation properties of SNM varied among the Bonn potentials at zero temperature, attributed to differences in the tensor force primarily provided by the pion, these variations did not markedly impact resulting neutron star properties, as evidenced in Figure 7.

Furthermore, the incorporation of finite-temperature effects introduced additional contributions to the system's pressure, resulting in a discernible increase in the mass peak for both nonrotating and rotating stellar models, as illustrated in Figure 8. Comparing the maximum mass of the zero-temperature EOS utilizing the Bonn B potential to the corresponding EOS at 70 MeV, we observe a comparable increase in mass for both nonrotating (19.1%), uniformly rotating (17.1%), and differentially rotating (21.4%) stellar sequences. This underscores the significance of temperature effects in neutron star models, particularly in delineating their mass and associated properties.

It is noteworthy that the EOS studied in this paper are sufficiently versatile to accommodate the mass of the most massive neutron star ever detected, PSR J0952–0607, estimated to be $2.35 \pm 0.17\, M_\odot$ (Bassa et al. 2017; Romani et al. 2022), and lead to masses and radii for PSR J0030+451 that are in agreement with the confidence intervals established for this pulsar (Miller et al. 2019).

As discussed in Section 4.3, the high maximum masses for both nonrotating and rotating stars resulting from the EOS in this paper are unsurprising as our implementation of the RBHF approximation is restricted to purely nucleonic matter. However, the inclusion of other baryons, specifically hyperons, is essential for a more realistic depiction of neutron star interiors and results in a softening of the EOS. While the theoretical framework used in this paper does not currently facilitate the study of hyperons in neutron star matter, we refer to the work

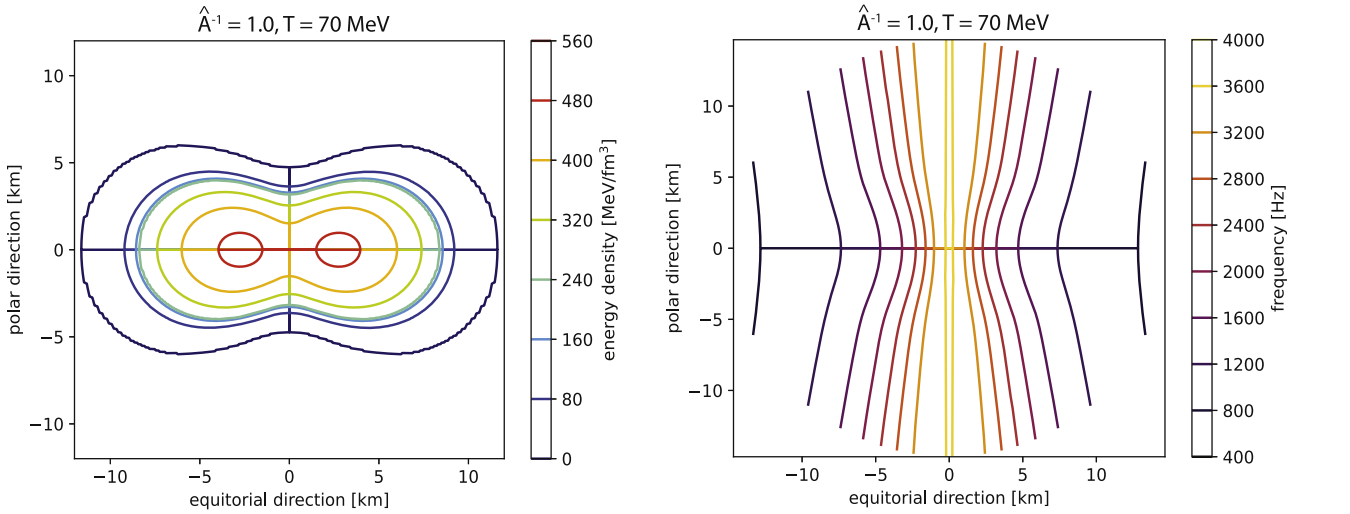

Figure 10. Energy density (left) and frequency (right) contours for a 2.89 $M_\odot$ differentially rotating star constructed using the EOS model from the Bonn B potential at $T = 70$ MeV. The star has a high degree of differential rotation, characterized by the rotation parameter $\hat{A}^{-1} = 1.0$.

of Katayama & Saito (2015) as an example of an implementation of the RBHF approximation that includes hyperons. However, it should be noted that the effect of negative-energy states of baryons is only partly accounted for, potentially explaining the significant deviations in nuclear matter properties such as energy per nucleon and compressibility from established values, which are well reproduced in our study. Consequently, direct comparison becomes complex. Despite this, viewing this study as a reference point, the inclusion of hyperons could potentially decrease the maximum mass of a purely nucleonic neutron star by approximately 15%–20%. Consequently, the maximum mass of the nonrotating neutron stars presented in this work would be reduced to around 2 $M_\odot$.

Acknowledgments

D.F. and F.W. are supported by the National Science Foundation (USA) under grant No. PHY-2012152.

ORCID iDs

Delaney Farrell https://orcid.org/0000-0003-1512-712X
Fridolin Weber https://orcid.org/0000-0002-5020-1906

References

Aad, G., Abat, E., Abdallah, J., et al. 2008, JInst, 3, P07007
Aasi, J., Abadie, J., Abbott, R., et al. 2015, CQGra, 32, 115012
Acernese, F. a., Agathos, M., Agatsuma, K., et al. 2014, CQGra, 32, 024001
Akmal, A., Pandharipande, V., & Ravenhall, D. 1998, PhRvC, 58, 1804
Baldo, M., & Burgio, G. 2016, PrPNP, 91, 203
Baldo, M., Robledo, L., Schuck, P., & Viñas, X. 2010, JPhG, 37, 064015
Bassa, C. G., Pleunis, Z., Hessels, J. W. T., et al. 2017, ApJL, 846, L20
Blaschke, D., & Chamel, N. 2018, in Phases of Dense Matter in Compact Stars, ed. L. Rezzolla et al. (Cham: Springee), 337
Brockmann, R., & Machleidt, R. 1990, PhRvC, 42, 1965
Carbone, A., & Schwenk, A. 2019, PhRvC, 100, 025805
Chesler, P. M., Jokela, N., Loeb, A., & Vuorinen, A. 2019, PhRvD, 100, 066027
Cook, G. B., Shapiro, S. L., & Teukolsky, S. A. 1992, ApJ, 398, 203
Cook, G. B., Shapiro, S. L., & Teukolsky, S. A. 1994, ApJ, 424, 823
Dutra, M., Lourenço, O., Avancini, S. S., et al. 2014, PhRvC, 90, 055203
Dutra, M., Lourenço, O., Sá Martins, J. S., et al. 2012, PhRvC, 85, 035201
Farrell, D., Alp, A., Weber, F., et al. 2023, New Phenomena And New States Of Matter In The Universe: From Quarks To Cosmos (Singapore: World Scientific), 199
Garg, U., & Colo, G. 2018, PrPNP, 101, 55
Garmire, G. P., Bautz, M. W., Ford, P. G., Nousek, J. A., & Ricker, G. R., Jr 2003, Proc. SPIE, 4851, 28
Gendreau, K. C., Arzoumanian, Z., & Okajima, T. 2012, Proc. SPIE, 8443, 844313
Hanauske, M., Takami, K., Bovard, L., et al. 2017, PhRvD, 96, 043004
Harrison, B. K., Thorne, K. S., Wakano, M., & Wheeler, J. A. 1965, Gravitation Theory and Gravitational Collapse (Chicago, IL: Univ. Chicago Press)
Hartle, J. B., & Thorne, K. S. 1968, ApJ, 153, 807
Huber, H., Weber, F., Weigel, M., & Schaab, C. 1998, IJMPE, 7, 301
Huber, H., Weber, F., & Weigel, M. 1995, PhRvC, 51, 1790
Katayama, T., & Saito, K. 2015, PhLB, 747, 43
Koliogiannis, P. S., & Moustakidis, C. C. 2021, ApJ, 912, 69
Laskos-Patkos, P., Koliogiannis, P. S., Kanakis-Pegios, A., & Moustakidis, C. C. 2022, Univ, 8, 395
Lattimer, J. M. 2019, Univ, 5, 159
Lattimer, J. M. 2023, Parti, 6, 30
Li, B.-A., Cai, B.-J., Chen, L.-W., & Xu, J. 2018, PrPNP, 99, 29
Li, B.-A., Cai, B.-J., Xie, W.-J., & Zhang, N.-B. 2021, Univ, 7, 182
Lyford, N. D., Baumgarte, T. W., & Shapiro, S. L. 2003, ApJ, 583, 410
Martin, P. C., & Schwinger, J. 1959, PhRv, 115, 1342
Miller, M., Lamb, F. K., Dittmann, A., et al. 2019, ApJL, 887, L24
Morrison, I. A., Baumgarte, T. W., & Shapiro, S. L. 2004, ApJ, 610, 941
Moustakidis, C. C., & Panos, C. P. 2009, PhRvC, 79, 045806
Müller, B., & Nagle, J. L. 2006, ARNPS, 56, 93
Negele, J. W., & Vautherin, D. 1973, NuPhA, 207, 298
Oertel, M., Hempel, M., Klähn, T., & Typel, S. 2017, RvMP, 89, 015007
Ou, S., Tohline, J. E., & Lindblom, L. 2004, ApJ, 617, 490
Perego, A., Bernuzzi, S., & Radice, D. 2019, EPJA, 55, 124
Poschenrieder, P., & Weigel, M. 1988, PhRvC, 38, 471
Ring, P., Wang, S., Zhao, Q., & Meng, J. 2021, EPJWC, 252, 02001
Roca-Maza, X., Centelles, M., Viñas, X., & Warda, M. 2011, PhRvL, 106, 252501
Romani, R. W., Kandel, D., Filippenko, A. V., Brink, T. G., & Zheng, W. 2022, ApJL, 934, L17
Schneider, A. S., Constantinou, C., Muccioli, B., & Prakash, M. 2019, PhRvC, 100, 025803
Sedrakian, A., Li, J.-J., & Weber, F. 2022, in Astrophysics in the XXI Century with Compact Stars, ed. C. A. Z. Vasconcellos & F. Weber (Singapore: World Scientific), 153
Sedrakian, A., Li, J. J., & Weber, F. 2023, PrPNP, 475, 104041
Shen, S., Liang, H., Meng, J., et al. 2017, PhRvC, 96, 014316
Spiller, P., & Franchetti, G. 2006, NIMPA, 561, 305
Spinella, W. M., & Weber, F. 2020, Topics on Strong Gravity: A Modern View on Theories and Experiments (Singapore: World Scientific), 85
Stergioulas, N. 2003, LRR, 6, 1

Stone, J., Stone, N., & Moszkowski, S. 2014, PhRvC, 89, 044316
ter Haar, B., & Malfliet, R. 1986, PhRvL, 56, 1237
ter Haar, B., & Malfliet, R. 1987, PhR, 149, 207
Tolman, R. C. 1939, PhRv, 55, 364
Tong, H., Ren, X.-L., Ring, P., et al. 2018, PhRvC, 98, 054302
Tong, H., Wang, C., & Wang, S. 2022, ApJ, 930, 137
van Dalen, E. N. E., Fuchs, C., & Faessler, A. 2007, EPJA, 31, 29
Wang, C., Hu, J., Zhang, Y., & Shen, H. 2020, ApJ, 897, 96
Wang, S., Zhao, Q., Ring, P., & Meng, J. 2021, PhRvC, 103, 054319
Weber, F. 1999, Pulsars as Astrophysical Laboratories for Nuclear and Particle Physics (Series in High Energy Physics, Cosmology and Gravitation) (1st ed.; New York: Routledge), doi:10.1201/9780203741719
Weber, F., & Glendenning, N. 1992, ApJ, 390, 541
Weber, F., Glendenning, N., & Weigel, M. 1991, ApJ, 373, 579
Wei, J.-B., Burgio, G. F., Raduta, A. R., & Schulze, H.-J. 2021, PhRvC, 104, 065806